AFRL-RD-PS-
TP-2021-0019

ULTRABROADBAND MICROWAVE RADIATION FROM NEAR AND MID-INFRARED LASER PRODUCED PLASMAS IN AIR

Alexander Englesbe, et al.

10 October 2020

Technical Paper

AIR FORCE RESEARCH LABORATORY
Directed Energy Directorate
3550 Aberdeen Ave SE
AIR FORCE MATERIEL COMMAND
KIRTLAND AIR FORCE BASE, NM 87117-5776

NOTICE AND SIGNATURE PAGE

Using Government drawings, specifications, or other data included in this document for any purpose other than Government procurement does not in any way obligate the U.S. Government. The fact that the Government formulated or supplied the drawings, specifications, or other data, does not license the holder or any other person or corporation; or convey any rights or permission to manufacture, use, or sell any patented invention that may relate to them.

This report was cleared for public release by the AFMC Public Affairs Office and is available to the general public, including foreign nationals. Copies may be obtained from the Defense Technical Information Center (DTIC) (http://www.dtic.mil).

AFRL-RD-PS-TP-2021-0019 HAS BEEN REVIEWED AND IS APPROVED FOR PUBLICATION IN ACCORDANCE WITH ASSIGNED DISTRIBUTION STATEMENT.

SCHMITT-SODY.ANDREAS.1292923151 Digitally signed by SCHMITT-SODY.ANDREAS.1292923151 Date: 2021.07.12 12:02:25 -06'00'

Andreas Schmitt-Sody, DR-III
Senior Research Engineer, AFRL/RDHP

LANGDON.STEPHEN.L.1232187065 Digitally signed by LANGDON.STEPHEN.L.1232187065 Date: 2021.07.12 12:15:30 -06'00'

Stephen Langdon, DR-III
Branch Chief, ARFRL/RDHP

This report is published in the interest of scientific and technical information exchange, and its publication does not constitute the Government's approval or disapproval of its ideas or findings.

REPORT DOCUMENTATION PAGE

Form Approved
OMB No. 0704-0188

1. REPORT DATE *(DD-MM-YYYY)*
10-10-2020

2. REPORT TYPE
Technical Paper

3. DATES COVERED *(From - To)*
N/A

4. TITLE AND SUBTITLE

ULTRABROADBAND MICROWAVE RADIATION FROM NEAR AND MID-INFRARED LASER PRODUCED PLASMAS IN AIR

5a. CONTRACT NUMBER
FA9451-20-F-0001

5b. GRANT NUMBER

5c. PROGRAM ELEMENT NUMBER

6. **AUTHOR(S)**

Alexander Englesbe, Jennifer Elle, Robert Schwartz, Travis Garrett, Daniel Woodbury, Dogeun Jang, Ki-Yong Kim, Howard Milchberg, Remington Reid, Adrian Lucero, Daniel Gordon, Ryan Phillips, Serge Kalmykov, Andreas Schmitt-Sody

5d. PROJECT NUMBER

5e. TASK NUMBER

5f. WORK UNIT NUMBER
D0G9

7. **PERFORMING ORGANIZATION NAME(S) AND ADDRESS(ES)**

Air Force Research Laboratory 3550 Aberdeen Ave SE Kirtland AFB, NM 87117-5776
Leidos, 2109 Air Park Rd SE, Albuquerque, NM 87106
University of Maryland, 8279 Paint Branch Drive College Park, MD 20742
Naval Research Laboratory,4555Overlook Ave., Washington, DC 20375

8. PERFORMING ORGANIZATION REPORT NUMBER

9. SPONSORING / MONITORING AGENCY NAME(S) AND ADDRESS(ES)

Air Force Research Laboratory
3550 Aberdeen Ave. SE
Kirtland AFB, NM 87117-5776

10. SPONSOR/MONITOR'S ACRONYM(S)
RDHP

11. SPONSOR/MONITOR'S REPORT NUMBER(S) AFRL-RD-PS-TP-2021-0019

12. DISTRIBUTION / AVAILABILITY STATEMENT
Approved for Public Release: Distribution Unlimited. AFMC-2020-0152,

13. SUPPLEMENTARY NOTES
Published Physical Review A

14. ABSTRACT

An ultrashort laser pulse focused in air creates a plasma that radiates broadband electromagnetic waves. We experimentally compare the generation of microwaves from plasmas produced with two different laser systems that operate in the near and mid-infrared regimes. Changing the laser wavelength increases the microwave power by 100 times, and changing the input pulse energy allows for tuning of the microwave frequency spectrum, which we absolutely calibrate over a range of 2-70 GHz. The variation of the spectrum with laser pulse energy confirms the existence of a distinct mechanism that generates microwave radiation from laser produced plasmas in gases. We propose that a radial diffusive expansion wave of the plasma electrons drives a longitudinal along the plasma surface whose amplitude varies with the total residual electron energy imparted by the laser field, and this longitudinal current produces the detected radiation.

15. SUBJECT TERMS
Laser filamentation, high intensity lasers, laser plasma, laser plasma dynamics,

16. SECURITY CLASSIFICATION OF:			**17. LIMITATION OF ABSTRACT**	**18. NUMBER OF PAGES**	**19a. NAME OF RESPONSIBLE PERSON** A. Schmitt-Sody
a. REPORT UNCLASSIFIED	**b. ABSTRACT** UNCLASSIFIED	**c. THIS PAGE** UNCLASSIFIED	NONE	42	**19b. TELEPHONE NUMBER** *(include area code)*

Standard Form 298 (Rev. 8-98)
Prescribed by ANSI Std. 239.18

This page left intentionally blank

Ultrabroadband microwave radiation from near and mid-infrared laser produced plasmas in air

Alexander Englesbe,[1] Jennifer Elle,[2] Robert Schwartz,[3] Travis Garrett,[2] Daniel Woodbury,[3] Dogeun Jang,[3] Ki-Yong Kim,[3] Howard Milchberg,[3] Remington Reid,[2] Adrian Lucero,[2] Daniel Gordon,[1] Ryan Phillips,[2] Serge Kalmykov,[2,4] and Andreas Schmitt-Sody[2]

[1]*Plasma Physics Division, Naval Research Laboratory, Washington, DC 20375*

[2]*High Power Electromagnetics Division,*
Air Force Research Laboratory, Kirtland AFB, NM 87117

[3]*Institute for Research in Electronics and Applied Physics,*
University of Maryland, College Park, MD 20742

[4]*Leidos Innovations Center, Albuquerque, NM 87106*

(Dated: May 28, 2021)

Abstract

An ultrashort laser pulse focused in air creates a plasma that radiates broadband electromagnetic waves. We experimentally compare the generation of microwaves from plasmas produced with two different laser systems that operate in the near and mid-infrared regimes. Changing the laser wavelength increases the microwave power by 100 times, and changing the input pulse energy allows for tuning of the microwave frequency spectrum, which we absolutely calibrate over a range of 2-70 GHz. The variation of the spectrum with laser pulse energy confirms the existence of a distinct mechanism that generates microwave radiation from laser produced plasmas in gases. We propose that a radial diffusive expansion wave of the plasma electrons drives a longitudinal current along the plasma surface whose amplitude varies with the total residual electron energy imparted by the laser field, and this longitudinal current produces the detected radiation.

I. INTRODUCTION

Ultrashort pulse laser-produced plasmas are versatile sources of secondary radiation, that is electromagnetic radiation arising from currents driven in the plasma by the laser pulse. For a laser pulse focused in gas, there are many possible mechanisms that have been closely studied that can cause emission above and below the laser frequency [1–5]. Low frequency secondary radiation at terahertz (THz) frequencies from plasmas generated in air has been investigated extensively with near-infrared (NIR) laser systems typically using two-color pulses [6, 7], and has more recently been measured using mid-infrared (MIR) laser drivers [8, 9]. However these plasmas also radiate at even lower frequencies in the microwave, that is gigahertz (GHz) regime [10–14]. The mechanism that causes emission on nanosecond timescales, which are much longer than the laser pulse duration ($\sim$ 100 fs) or plasma frequency ($2\pi/\omega_p \sim 1$ ps) has not been identified by prior investigations.

This paper reports the results of a systematic experimental study of the microwave generation from air plasma in the spectral range of 2 to 70 GHz. The plasma emitting the microwaves is created by optical field ionization with NIR ($\lambda_0 = 0.8$ μm) or MIR ($\lambda_0 = 3.9$ μm) pulses focused in ambient air.

The experiments accomplish two purposes. First, we show that the microwave amplitude and frequency may be tuned by changing the laser wavelength and pulse energy, respectively. We measure a 100-fold increase in the emitted microwave power merely by increasing the

laser wavelength while keeping the focusing optics and laser pulse energy the same. When we increase the laser energy at both wavelengths, we find that the peak microwave frequency decreases. Second, these results prove that the microwaves arise from a distinct generation mechanism which we explain for the first time, and is supported by simulations of the ionization caused by the laser propagation.

As the laser pulse passes, the electrons near the boundary of the plasma column produced by the intense field expand radially outwards in a conical shell due to their residual energy. The residual energy is the electron energy distribution imparted by the laser field to the electron population [15–18]. The highest energy component of the distribution scales with laser intensity and wavelength like $I_0\lambda_0^2$ (for further discussion see Supplementary Section 1[19]). The conical expansion of the electrons evolves over a timescale on the order of 100 ps (which corresponds to the microwave frequencies we measure) and its asymmetry in the direction of the laser propagation stimulates a longitudinal surface current on the outer boundary of the finite conductivity plasma column. This surface current travels coherently behind the ionizing laser pulse, thereby building up a radially polarized electromagnetic wave. The wave then detaches from the end of the plasma column and propagates into the far field as a broadband microwave pulse.

Pulsed microwaves with bandwidth as large as we have observed in these experiments can usually only be achieved with microwave photonic devices (see for example [20]). Creating them by other means involves complicated microwave circuit design techniques such as a photoconductive resonator [21], a pulse forming network that shortens a longer duration pulse [22], or a specialized monolithic microwave integrated circuit (MMIC) [23]. The plasmas are able to provide comparable or greater bandwidth and a large tuning range simply by tightly focusing high-intensity femtosecond laser pulses in air.

To date, experimental observations of radiofrequency and microwave radiation from laser plasmas are usually associated with the interaction of nanosecond to femtosecond pulses with solids (see for example Refs. [24–27]). We find the cause of the microwave radiation from the air plasma to be physically dissimilar from that in laser-solid interactions, although in both cases the source currents can be considered to arise from the high energy tails of the respective electron energy distributions in the laser produced plasmas [28, 29].

II. EXPERIMENTAL METHODS

The MIR laser in our experiments uses staged optical parametric chirped pulse amplification (OPCPA) to produce ultrashort pulses centered at $\lambda_0 = 3.9$ μm with a duration of approximately 100 fs at a repetition rate of 20 Hz [30]. The NIR experiments are performed on a traditional Ti:sapphire chirped pulse amplification (CPA) system with $\lambda_0 = 0.8$ μm, and a 50 fs pulse duration operating at 10 Hz. The uncertainty in the pulse durations for both lasers is about 10%. Figure 1 shows the setup for both the NIR and MIR microwave generation experiments.

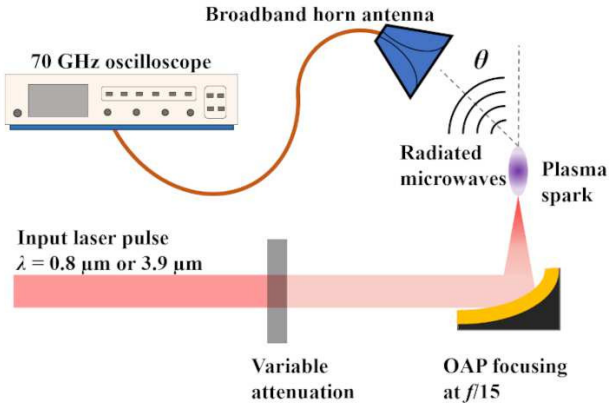

FIG. 1. Experimental setup for measuring microwave radiation from the laser sparks in air. The horn antenna translates angularly around the plasma at a fixed radius. An angular antenna position of $\theta = 0^\circ$ corresponds to the laser axis.

A diaphragm iris at the laser outputs limits their apertures to a 10 mm diameter. The iris provides a circular shape to the transverse profile of the MIR laser so that the laser conditions are closer to those of the NIR laser. The apertured MIR pulses have some transverse structure, which will decrease the maximum focal intensity relative to an ideal Gaussian beam. The energy of the input pulses at $\lambda_0 = 0.8$ μm and 3.9 μm is set within a range from 2-12 mJ, with a typical shot-to-shot fluctuation of 10%. An off-axis parabolic mirror (OAP) with a 150 mm reflected focal length focuses the pulses at $f/15$ to make a plasma spark that is ≤ 1 cm in length. While the f-number and input pulse energies are standardized between the two laser systems, it was necessary to shorten the pulse duration of the NIR laser relative to the MIR laser in order to produce measurable signal levels from

the NIR laser plasma. This is why the NIR laser pulse duration is 50 fs, whereas it is 100 fs for the MIR laser.

Our experimental setup is sufficient to demonstrate that the laser wavelength can significantly influence the production of the microwave radiation. However, to experimentally measure the precise scaling of the microwave power with laser wavelength and intensity as it relates to the electron residual energy, one would have to account for the wavelength dependence of the beam waist and the resulting plasma diameter by carefully controlling the characteristics of the input laser pulses. Nonetheless, our simulations of the laser propagation in these experiments show that the beam waist and plasma diameter are largely similar for the MIR and NIR laser pulses (the simulations assume ideal input beam quality). It is important to note that since we have used a 10 mm diameter beam incident on a 150 mm focal length OAP at both values of λ_0, the ideal vacuum spot diameter and therefore intensity through the focal region have wavelength dependence. For a Gaussian transverse intensity profile, the Rayleigh range and focused spot diameter in vacuum both scale with λ_0, and therefore the intensity scales with λ_0^{-2}. In atmosphere, plasma-induced de-focusing and nonlinear self-focusing due to the Kerr effect determine the focal intensity and spot size. These effects are accounted for in the laser propagation simulations.

The bandwidth of the microwave pulses radiated from the air plasmas is so broad that it is impractical to measure the radiation in a single laser shot. We use four standard broadband horn antennas to cover the complete frequency range from 2-70 GHz. A Tektronix DPO77002SX with 70 GHz real time bandwidth digitizes the microwave waveforms. The oscilloscope sets the upper frequency limit of our measurements, and each horn antenna operates in a subrange of its total bandwidth (2-18 GHz, 18-40 GHz, 40-60 GHz, and 50-70 GHz). The spectral and waveform amplitude measurements are averaged from hundreds of laser shots.

Each antenna is mounted on a rotating gantry at a fixed distance of 55 cm from the plasma, which was the maximum achievable given the space constraints in the laboratory. Spectral-angular maps of the microwaves are recorded using both laser systems by translating each antenna about the plasma in 10° increments from close to the laser axis at $\theta \simeq 0°$ to its normal at 90°. Reflections of the microwaves off any nearby surfaces are either damped with microwave absorbing foam, or discriminated by time of flight since the pulse duration is very short. The antennas are used in succession in an attempt to keep constant the orientation

between their apertures and the plasma at each observation angle. Our measurements rely on the high shot-to-shot repeatability of the microwave radiation. The shot-to-shot variance in the microwave waveform amplitude is determined by the fluctuation in the laser pulse energy.

There is a unique response function for each antenna and the coaxial cable connecting it to the oscilloscope. The spectrum from each must be absolutely calibrated in order to present spectra as if they were measured with a single instrument having uniform frequency response. We used reference noise sources that produce known microwave power spectral densities to measure the real part of the response function to calculate calibration factors for each coaxial cable with the oscilloscope. The four antennas are calibrated separately using the two antenna technique [31] to measure their gain as a function of frequency. We did not measure the full complex transfer functions, so we cannot combine the different antenna waveforms in the time domain, which is why Figures 2 and 3 use uncalibrated data. Further details describing how to perform the calibrations are given in the Supplementary Section 2.

III. RESULTS

A. Waveforms and Amplitudes in the Time Domain

We find signal over the entire frequency range accessible to the four horn antennas we used to collect the radiation. For a single laser pulse energy and antenna observation angle, Figure 2 shows the time domain voltage waveforms with each of the antennas. There is a measurable, few-cycle microwave pulse in every case whose duration is about 500 ps. The waveforms appear to be negatively chirped. Horn antennas are dispersive, having complicated frequency-dependent phase responses [32] (over the broad frequency ranges the coaxial cables will also contribute dispersion) which likely cause the apparent chirp and the multiple oscillations of the waveforms. That is, the instrument response given by each combination of antenna and coaxial cable with the oscilloscope significantly influences the detailed structures of the waveforms in Figure 2.

One main result of the experiments is the large amplitude difference between the MIR and NIR laser produced microwaves. The amplitude difference can be found at any emission angle from the plasma, as shown in Figure 3, which compares the waveform peak-to-peak voltage,

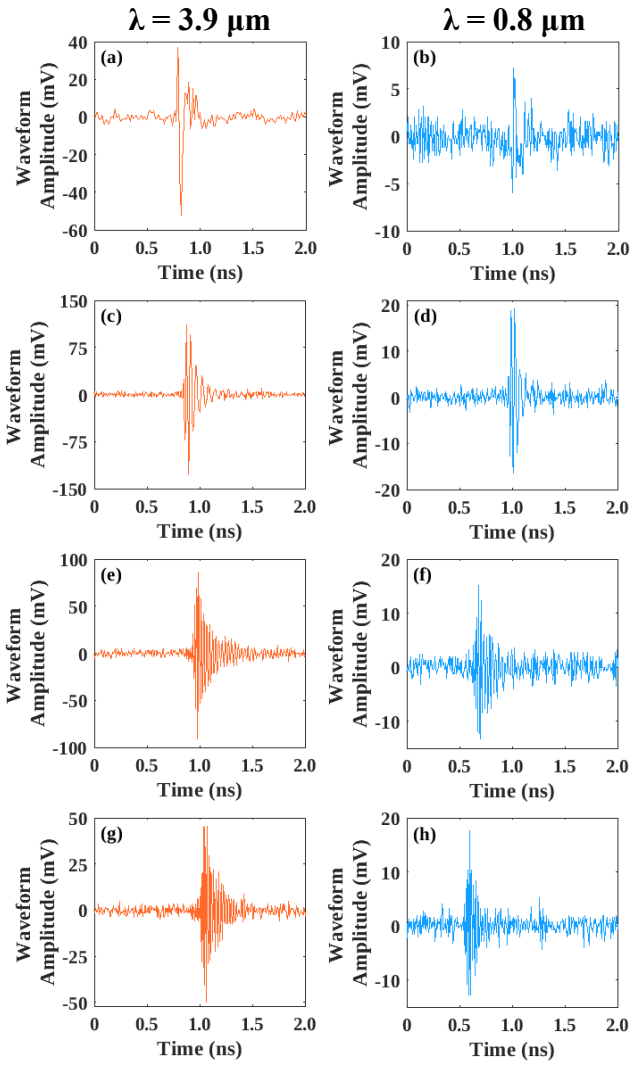

FIG. 2. Time domain voltage waveforms of the microwave fields radiating from the air plasmas at a constant laser pulse energy of 12 mJ. The fields are received with antennas operating at (a),(b) 2-18 GHz, (c),(d) 18-40 GHz, (e),(f) 40-60 GHz, and (g),(h) 50-70 GHz. For the left column of plots $\lambda_0 = 3.9$ μm, and in the right column, $\lambda_0 = 0.8$ μm. The horns are located at $\theta = 30°$ off the laser axis. The time axis in each plot is based on an arbitrary reference for time $t = 0$, as the trigger signal cable lengths are different for both of the lasers, and the microwave cables used with each of the horns also do not all have the same length.

V_{pp}, as a function of the angular position of the antennas, θ, at a fixed laser energy of 2 mJ. Direct comparison of the time domain amplitudes between the cases of laser wavelength is only valid for an individual antenna and accompanying coaxial cable (as opposed to

comparing, for example, V_{pp} for 2-18 GHz with that for 50-70 GHz). The order of magnitude

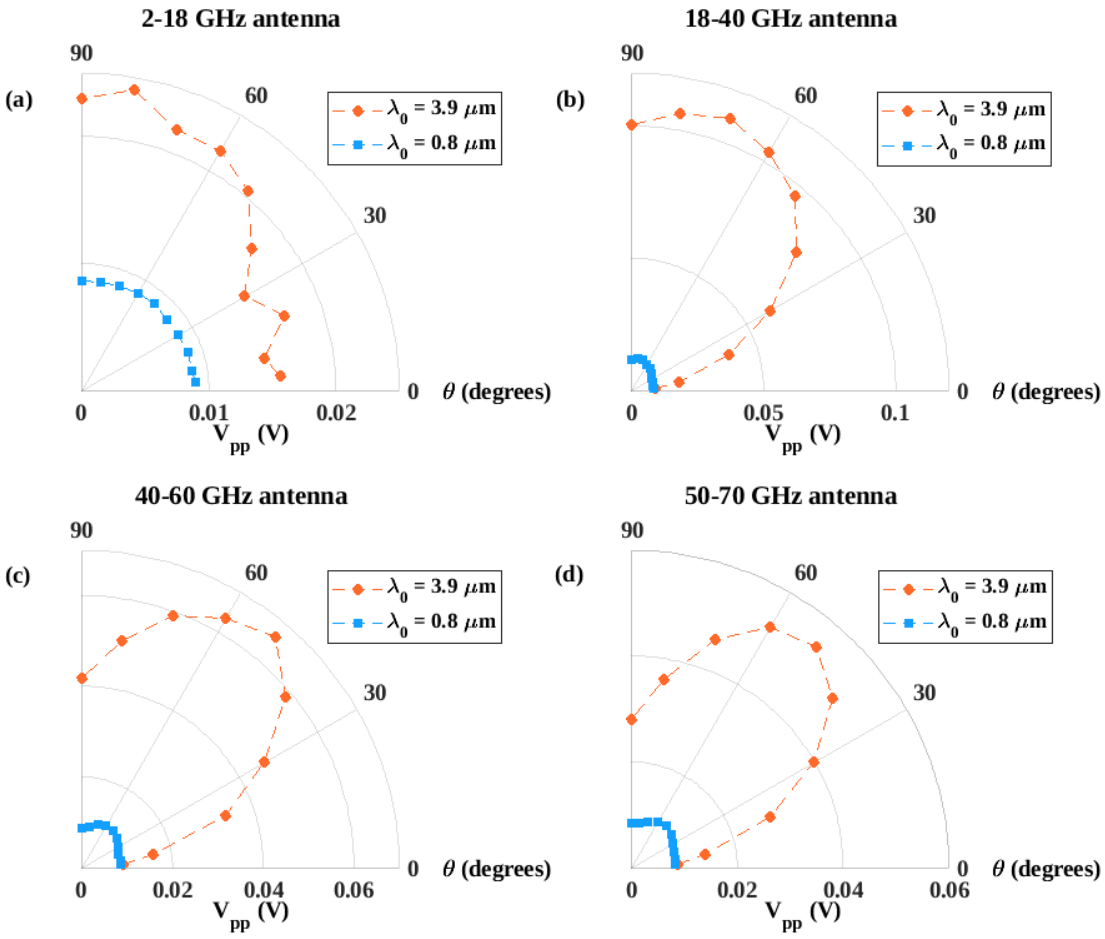

FIG. 3. Polar plots of the angular pattern of the radiation based on V_{pp} for voltage waveforms recorded with the (a) 2-18 GHz, (b) 18-40 GHz, (c) 40-60 GHz, and (d) 50-70 GHz antennas. The orange circles and blue squares correspond to $\lambda_0 = 3.9$ μm and $\lambda_0 = 0.8$ μm, respectively, at a laser pulse energy of 2 mJ. The laser propagates from left to right.

increase in V_{pp} is observed over the range of emission angles and antenna frequency ranges. V_{pp} is proportional to the microwave electric field amplitude, and therefore V_{pp}^2 is proportional to the microwave power. This means that the MIR laser produced plasma radiates on the order of 100 times the total microwave power of the plasma generated by the NIR laser.

Another characteristic to note is the shape of the angular distributions. The radiation is cylindrically symmetric about the laser propagation axis, even though Figure 3 plots the angular dependence of V_{pp} in the plane formed by the microwave electric field vector and the laser propagation direction. Figures 3(b)-(d) indicate that the microwaves radiate in

a forward-directed cone, with the angle of maximum emission occurring between the laser propagation axis ($\theta = 0°$) and its normal ($\theta = 90°$). There is some frequency dependence to the peak emission angle. Comparison of Figures 3(b) and 3(d), for example shows that while the peak emission angle in the 18-40 GHz frequency range is $\theta \sim 70°$, it is $\theta \sim 50°$ in the 50-70 GHz range. The conical radiation pattern whose maximum becomes more forward-directed at higher frequencies implies that the current that produces the radiation flows parallel to the laser propagation axis, and that it has a phase velocity approaching the group velocity of the laser pulse in the plasma. In general, a conical emission pattern with a null on axis is found for an electric dipole accelerating parallel to its dipole moment [33].

The polarization of the microwave electric field is also consistent with a longitudinal plasma current. In a cylindrical coordinate system, a longitudinal current produces an azimuthal magnetic field, which means that the electric field is radially polarized. We observed horizontal polarization of the microwaves in the plane of the measurements, and vertical polarization at an azimuthal position displaced 90° from the measurement plane. The antennas are linearly polarized, so the signal amplitude is maximized when the angular difference between the incoming electric field vector and the antenna polarization (its E-plane) is minimized. We check for the microwave polarization by rotating the apertures of the horn antennas by 90°, similar to how one would use a linear polarizer to observe the polarization of optical light.

B. Laser Pulse Energy Dependence of the Microwave Power

For both laser wavelengths, the radiated microwave power as a function of the input laser pulse energy increases at roughly the same rate over the range we used in the experiments. Instead of presenting measurements of V_{pp}, Figure 4 shows the relative change in the total power integrated from 2-70 GHz radiated per steradian as a function of laser energy. The measurement is repeated at three different observation angles. The total power is found by applying the calibration factors to the uncalibrated frequency spectra to get the absolute electric field spectrum, squaring it, and then integrating the result, which is a quantity proportional to the radiated power ($\int E^2 df \propto dP/d\Omega$, where E is spectral field amplitude, P is power, and Ω is solid angle). The data in each plot are normalized to the power of the MIR-produced microwaves at a laser energy of 12 mJ.

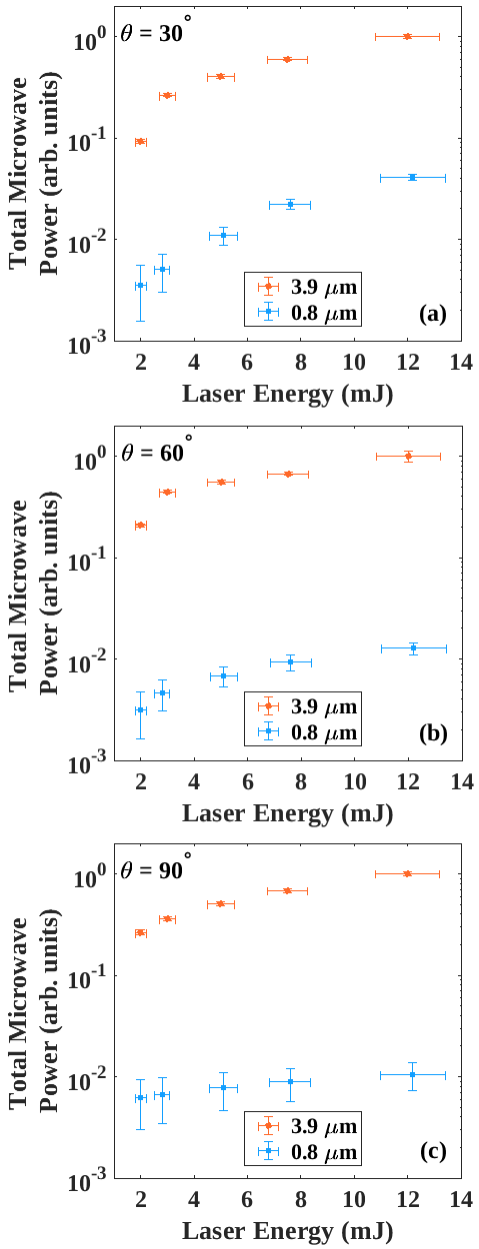

FIG. 4. Normalized total power integrated from 2-70 GHz at each value of laser pulse energy at both laser wavelengths. The position of the antennas in each set of measurements is (a) $\theta = 30°$, (b) $\theta = 60°$, and (c) $\theta = 90°$. The error bars are calculated by finding the standard deviation of each electric field frequency component, adding these in quadrature since each normalized total power data point represents a numerical integration, and dividing by the number of frequency components in the spectrum.

Figures 2-4 show different, complementary measurements to prove that the total mi-

crowave power radiated from the MIR laser plasma is two orders of magnitude greater than that due to the NIR laser plasma. While the power also increases with input laser pulse energy, it appears that the wavelength dependence is stronger.

Increasing the laser pulse energy by a factor of 6 (from 2 to 12 mJ) results in a similar increase in the total power. However, at a given laser pulse energy, increasing the wavelength by a factor of 5 results in 100 times the total power. The pulse energy and wavelength dependence we measure reflect the $I_0\lambda_0^2$ scaling of the electron residual energy, although other laser intensity and wavelength-dependent factors such as the plasma volume also play a role to determine the microwave power.

C. Absolutely Calibrated Microwave Frequency Spectra

Figure 5 shows the absolutely calibrated microwave spectra as a function of laser pulse energy. The spectra are the electric field amplitude in free space at the location of the antenna aperture. Their bandwidth is typically greater than 100%, although each one contains a clear frequency peak. Observing the peaks would not be possible without calibrating the receivers. They have inverse dependence on the laser energy for both $\lambda_0 = 3.9$ μm and $\lambda_0 = 0.8$ μm. Therefore the laser energy is also a means for tuning the microwave frequency content in these experiments.

The inverse laser pulse energy dependence of the frequency peaks proves that the microwaves arise from a distinct generation mechanism. We hypothesize that the peak frequency is related to the length of the laser plasma, which increases with the laser pulse energy. For the focusing f-number and laser energies we have used, the frequency spectra reach their peak in the range of 10's of GHz.

Existing models for THz radiation from laser plasmas in air predict that its spectrum peaks in the THz at the plasma frequency [14, 34–37]. They assume longitudinal charge separation in the core of the plasma driven by inverse bremsstrahlung and the ponderomotive force. The photocurrent model is predicated upon a two-color laser driver [4], and is not predicted to produce significant microwave radiation at atmospheric pressure [38]. Our experiments only involve single color pulses at the lasers' fundamental wavelengths, and the results are not accounted for by the predictions of existing models.

The microwave generation should be considered an effect that is independent from the

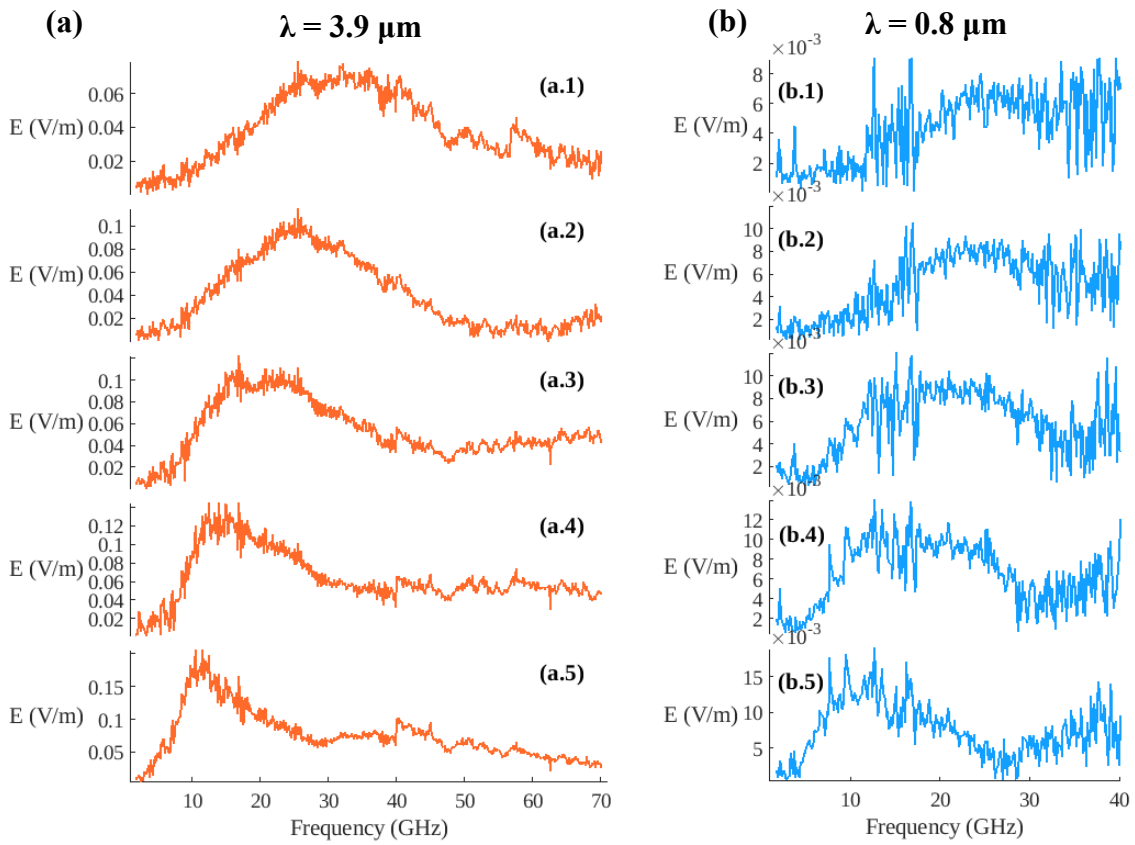

FIG. 5. Calibrated spectra of the free-space microwave electric field radiating from the air plasmas as a function of laser pulse energy. The antennas are positioned at $\theta = 90°$ relative to the laser propagation axis. The two columns of spectra correspond to the different lasers with (a) $\lambda_0 = 3.9$ μm, and (b) $\lambda_0 = 0.8$ μm. The sub-plots within (a) and (b) are numbered 1-5, corresponding to laser pulse energies of 2, 3, 5, 7.5, and 12 mJ, respectively. The spectra in (b) have been truncated at 40 GHz because the noise rises above the signal. The noise amplitude increases linearly with frequency when the calibration factors are applied. The signal-to-noise ratio in (a) is much larger and therefore the spectra do not have this limitation.

THz. In addition to the fact that the peaks we have measured are at much lower frequencies, the plasma frequency scales with square root of the electron density. The maximum electron density is determined by the ionization rate, which has a strong dependence on the magnitude of the laser electric field. If the microwave frequency content were determined by the plasma frequency as is the case for the THz, we would observe the opposite trend for the

peaks with increasing laser energy in Figure 5. Further, if the microwaves we measure were simply the low-frequency tail of the THz spectrum, then we would expect to observe in the microwave range a continuous spectrum increasing in amplitude up to the frequency limit of our receivers, and not the spectral peaks that we did find. Therefore, the microwave radiation mechanism must be different from that which produces THz radiation often observed from air plasmas made with ultrashort laser pulses.

IV. DISCUSSION

A. Microwave Generation Mechanism

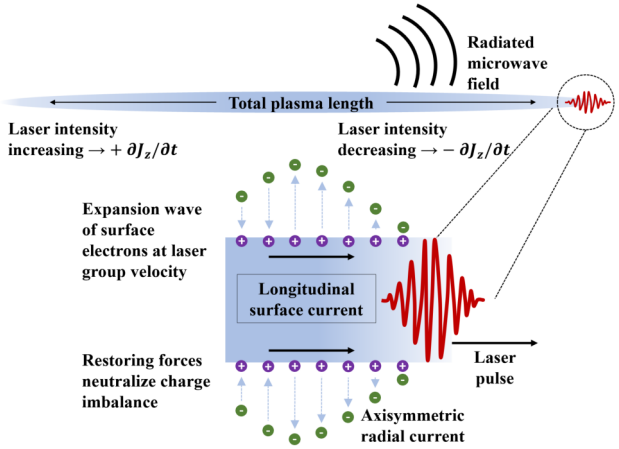

FIG. 6. A diagram describing the microwave radiation mechanism. The laser pulse propagates from left to right. The top portion of the figure shows the macroscopic picture of the slowly varying laser intensity and plasma properties that produce a current modulation on microwave timescales. The dashed lines indicate what occurs on a microscopic scale in the vicinity of the laser pulse as it propagates. The vertical arrows extending radially from the plasma point in the direction of the radial electron velocity. While it is initially outward, electrostatic attraction from the plasma draws the electrons back, indicated by the change in the arrows' direction. Collisions with neutrals serve as an additional restoring force that ultimately neutralizes the charge imbalance.

We propose that the microwave radiation is due to the time asymmetry of the radial expansion of the outer shell of electrons from the plasma column. Owing to their residual energy, the electrons begin diffusive expansion out into the surrounding neutral atmosphere

as soon as they are ionized. In atmosphere, elastic electron collisions with neutrals and ions moderate the expansion. By time asymmetry, we mean that the older electrons at the beginning of the plasma column will have expanded further than the younger electrons right behind the laser pulse, which leads to a conical profile for the expanding shell. The consequence of the conical profile is that the electron expansion is axisymmetric - at each moment in time every radial component of the electric field around the circumference of the plasma column is opposed by another component of equal magnitude on the opposite side. Therefore, the accompanying radial current produces no radiation that can propagate to the far field, even though the electrons experience acceleration in the radial direction over the rise time of the expansion wave. However, there is no such symmetry in the longitudinal direction. The rising and falling portions of the wave, that is the initial expulsion and subsequent relaxation of electrons from the plasma column surface, are temporally and spatially non-uniform.

This asymmetry will thus drive a pulse of longitudinal surface current in the direction of laser propagation, and this generates the broadband microwave signal. The longitudinal current pulse will be modulated over the length of the plasma column by the varying intensity of the laser pulse as it focuses and diffracts, and this in turn modifies the waveform of the resulting microwave field. The current modulation is what we believe causes the spectral shift we note in Figure 5 as the spatial profile of the plasma varies with the input laser pulse energy. Additional data linking the current modulation to the plasma shape is given in Supplementary Section 3.

Figure 6 illustrates the process. On the macroscopic level, that is one where the total length of the plasma is the relevant length scale, the longitudinal current increases and decreases in magnitude with the amplitude of the electron expansion wave that travels coherently behind the laser pulse. For longitudinally short plasmas generated under tight focusing conditions such as in these experiments, we find that this current modulation significantly influences the resulting microwave spectrum within the 2-70 GHz bandwidth of our measurements. On the other hand, we have observed in other experiments conducted in a limited bandwidth of 2-14 GHz with longitudinally extended plasmas where nonlinear propagation of the laser is more pronounced, that the microwave spectrum changes weakly with the plasma length [12]. The qualitative difference of these observations arises from the dependence of the coherent build-up of the microwaves on the plasma shape, and is discussed

further in Supplementary Section 3.

A prior experiment performed by Proulx, *et al.* [39] also implies an amplitude modulation of the electron expansion wave over the plasma length. Near field measurements of radiofrequency voltage waveforms induced on the exposed end of a coaxial cable held 0.5 cm from an approximately 20 cm-long filament-produced plasma increased in amplitude, then diminished and reversed polarity as the antenna translated longitudinally. While the receiver's 1 GHz maximum frequency would have significantly filtered the time evolution of the electric field, it is likely that the near field measurements and the radiation we have measured are aspects of the same phenomenon. The reported characteristic length scale of the longitudinal variation of the near field amplitude approaches the plasma length, which agrees with our description of how the electron expansion wave varies slowly in amplitude on the macroscopic scale.

On the microscopic scale (i.e. the bottom of Figure 6) we are concerned with the electron trajectories in and immediately following the laser pulse. For a given intensity, we expect that the λ_0^2 dependence of the residual energy causes the conical electron expansion wave to carry a larger radial current. Since the amplitude of the longitudinal surface current is determined by that of the radial expansion wave, the microwave radiation power should increase with laser wavelength, which is what we have quantified in Figures 2-5. Theory and simulations of the microwave generation mechanism that capture these microscopic and macroscopic scales of the plasma dynamics will be reported in a forthcoming publication [40].

B. Laser Propagation Simulations

To further support the idea that the λ_0^2 wavelength scaling of the residual energy is what drives the difference in microwave power between the MIR and NIR laser pulses, we performed simulations of the laser propagation to estimate the typical electron density and laser fluence of the experiments. The purpose of these simulations is to point out that the MIR laser plasma generates greater microwave power in spite of the fact that the peak intensity (see Supplementary Section 4) of the MIR pulses is predicted to be half that of the NIR pulses, and the number of available charge carriers is almost 100 times smaller. Therefore the residual electron energy must largely account for microwave signals we measured.

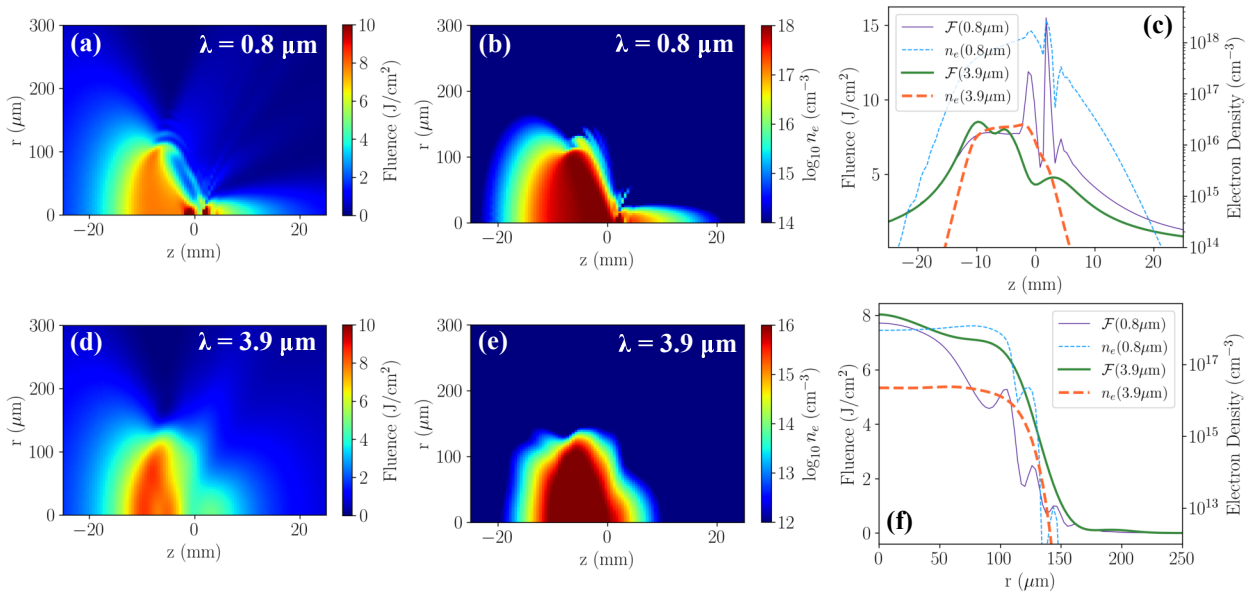

FIG. 7. Simulated laser fluence and electron density maps for 5 mJ input pulses focused at $f/15$. (a) Fluence and (b) electron density for $\lambda_0 = 0.8$ μm at 50 fs pulse duration. (d) Fluence and (e) electron density for $\lambda_0 = 3.9$ μm at 100 fs pulse duration. Note the difference in the electron density color bar limits for panels (b) versus (e). (c) Axial lineouts ($r = 0$) of the fluence ($\mathcal{F}$) and electron density (n_e) for both laser wavelengths. (f) Radial lineouts at $z = -5$ mm, which is where the plasma has the greatest radial extent. The thin solid and dashed lines correspond to fluence and electron density for $\lambda_0 = 0.8$ μm, respectively, while the heavy solid and dashed lines correspond to $\lambda_0 = 3.9$ μm. The longitudinal position $z = 0$ is at the geometric focal plane of the focusing optic.

The simulations use the propagation code SeaRay [41], which solves the unidirectional pulse propagation equation (UPPE) [42] in cylindrical symmetry. They account for the nonlinear air response due to the Kerr effect, ionization, and group velocity dispersion. SeaRay cannot simulate the plasma dynamics but it does calculate the electron density based on the tunneling ionization rate given by the PPT model [43].

The input pulses are transform limited and Gaussian in space and time (with durations of 50 fs for the NIR pulses and 100 fs for the MIR pulses) having phase fronts initialized with only the $f/15$ focusing of the OAP. The Gaussian envelope profile and initial phase front curvature are approximations that simplify the simulations, and do not reflect the detailed

structure of the intensity and phase of the input pulses in the experiments. However, the difference in wavelength ultimately dominates the plasma generation. The radial spatial increment is $\Delta r = 30$ μm, while the time step is sufficiently small to resolve the carrier frequency determined by each value of λ_0. The fluence and electron density are stored in longitudinal increments of $\Delta z = 500$ μm, although the simulation adaptively increments the longitudinal step while running. We used values for the nonlinear refractive index of $n_2 = 3.2 \times 10^{-19}$ cm^2/W for $\lambda_0 = 0.8$ μm [44], and $n_2 = 7.6 \times 10^{-20}$ cm^2/W for $\lambda_0 = 3.9$ μm [45]. We assume that the pulses ionize molecular oxygen, which is the dominant source of free electrons in air plasmas generated by strong laser fields [46], owing to its lower ionization potential of 12.1 eV versus 15.6 eV for molecular nitrogen. The simulations were performed over a range of input pulse energies that overlaps that of the experiments.

Figure 7 maps the laser fluence and electron density for 5 mJ NIR and MIR pulses as a function of propagation distance and radius, where $r = 0$ is the laser axis and $z = 0$ is the location of the geometric focus. The simulations show that the plasma causes the pulses to start defocusing before the geometric focus, which is expected because its refractive index is less than unity. The pulse evolution is more complicated in the NIR case, since it is above the self-focusing critical power, and therefore elicits a significant nonlinear response of the air. The ratio of input to critical power is $P/P_{cr} \sim 10$, where $P/P_{cr} = 1$ is the self-focusing threshold. $P_{cr} \propto \lambda_0^2/n_2$, where n_2 is the nonlinear refractive index. The MIR pulse power is well below the threshold ($P/P_{cr} \sim 0.2$), and does not exhibit significant nonlinear propagation.

Axial and radial lineouts of the laser fluence and electron density are given in Figures 7(c) and (f). Quantitatively, the on-axis laser fluence is similar between the NIR and MIR cases, although abrupt jumps in the fluence and electron density that accompany nonlinear collapse of the NIR pulse are clear in Figure 7(c). Comparison of the electron densities in the maps and lineouts shows that the NIR pulses generate a plasma that has about 100 times greater electron density than the MIR laser plasma. The NIR simulations predict detailed structure of the electron density due to the nonlinear propagation in Figures 7(c) and (f) that might result in complicated plasma dynamics after the laser pulse passes. It is not clear from our experimental microwave data whether this affects the radiation source, that is the diffusive expansion wave driving the longitudinal current pulse at the plasma surface.

In light of the microwave generation mechanism proposed above, we can make a few

observations relating to the microwave radiation even though there are no plasma dynamics in the simulations. Bear in mind that the plots of the simulation data represent a time-integrated picture of the laser propagation and ionization, and do not include for example, extinction of the plasma by recombination. The plasma size estimated as a fraction of the peak on-axis density appears to be about the same between the MIR and NIR cases. Figures 7(b),(e), and (f) indicate the maximum plasma radius is about 150 microns for both wavelengths. The cross-sectional area of plasma through which the microwave-producing currents flow ($I = \int \mathbf{J} \cdot d\mathbf{A}$) will contribute to the radiation amplitude, and since the plasma sizes are rather similar, we cannot completely attribute the factor of $\sim$ 100 difference in the experimentally measured microwave power to wavelength dependence the plasma size. The simulations together with our experimental data imply that if the MIR and NIR laser plasmas are about the same size, and the MIR plasma has orders of magnitude less bulk electron density, then the kinetic energy of the electrons is likely the primary factor causing the difference we measure in the microwave radiation power.

V. CONCLUSION

Our experiments show that we are able to control the amplitude and frequency content of broadband microwave pulses generated by focusing ultrashort laser pulses in air through the laser wavelength and pulse energy. To the best of our knowledge, these experiments are the first to compare the laser wavelength dependence of the microwave generation, although the wavelength scaling of THz generation has been explored previously in simulations and experiments [47–49]. Whether or not the increase in the microwave power as a function laser wavelength holds continuously over large ranges of λ_0 is not known, as many factors, such as molecular absorption of the laser by air constituents will affect the ionization and laser propagation [50]. While we used two different lasers to access the NIR and MIR regimes, wavelength tunable OPA-based ultrashort pulse lasers with millijoule pulse energies are proliferating, which would allow for tuning of the microwaves without needing wholly different laser infrastructure. The air plasmas may prove to be useful sources of microwave radiation for ultrabroadband single shot and pump-probe spectroscopy for measuring material properties in a frequency regime that is traditionally difficult to access, but of growing technological significance.

In addition to demonstrating control of the secondary radiation, we propose a novel generation mechanism that explains our experimental results, and is supported by modeling of the laser propagation and plasma generation. Our findings validate the notion that the electron residual energy ultimately drives the plasma currents that produce the microwaves. Direct simulation of the microwave generation across the multiple relevant temporal and spatial scales is part of our ongoing research.

ACKNOWLEDGMENTS

A.E. thanks Hugh Pohle for assistance with performing the antenna gain measurements for the receiver calibrations.

This material is based upon work supported by the Air Force Office of Scientific Research under award numbers FA9550-16RDCOR325, FA9550-19RDCOR027, FA9550-16-10121, and FA9550-16-10259. The research was performed while R. P. held an NRC Research Associateship Award at AFRL. D. W. acknowledges support from the DOE NNSA SSGF program under award DE-NA0003864. A.E. acknowledges support from the U.S. Naval Research Laboratory through the Jerome and Isabella Karle Postdoctoral Fellowship.

[1] B. Miao, L. Feder, J. Elle, A. J. Goers, D. Woodbury, F. Salehi, J. K. Wahlstrand, and H. M. Milchberg, Coherent ultra-broadband laser-assisted injection radiation from a laser plasma accelerator, Phys. Rev. E **98**, 043206 (2018).

[2] T. Matsuoka, C. McGuffey, P. G. Cummings, Y. Horovitz, F. Dollar, V. Chvykov, G. Kalintchenko, P. Rousseau, V. Yanovsky, S. S. Bulanov, A. G. R. Thomas, A. Maksimchuk, and K. Krushelnick, Stimulated raman side scattering in laser wakefield acceleration, Phys. Rev. Lett. **105**, 034801 (2010).

[3] A. Rundquist, C. G. Durfee, Z. Chang, C. Herne, S. Backus, M. M. Murnane, and H. C. Kapteyn, Phase-matched generation of coherent soft x-rays, Science **280**, 1412 (1998).

[4] K. Y. Kim, J. H. Glownia, A. J. Taylor, and G. Rodriguez, Terahertz emission from ultrafast ionizing air in symmetry-broken laser fields, Opt. Express **15**, 4577 (2007).

[5] X. Xie, J. Dai, and X.-C. Zhang, Coherent control of THz wave generation in ambient air,

Phys. Rev. Lett. **96**, 075005 (2006).

[6] K. Y. Kim, A. J. Taylor, J. H. Glownia, and G. Rodriguez, Coherent control of terahertz supercontinuum generation in ultrafast laser-gas interactions, Nat. Photon. **2**, 605 (2008).

[7] V. A. Andreeva, O. G. Kosareva, N. A. Panov, D. E. Shipilo, P. M. Solyankin, M. N. Esaulkov, P. González de Alaiza Martínez, A. P. Shkurinov, V. A. Makarov, L. Bergé, and S. L. Chin, Ultrabroad terahertz spectrum generation from an air-based filament plasma, Phy. Rev. Lett. **116**, 063902 (2016).

[8] D. Jang, R. M. Schwartz, D. Woodbury, J. Griff-McMahon, A. H. Younis, H. M. Milchberg, and K.-Y. Kim, Efficient terahertz and Brunel harmonic generation from air plasma via mid-infrared coherent control, Optica **6**, 1338 (2019).

[9] A. D. Koulouklidis, C. Gollner, V. Shumakova, V. Y. Fedorov, A. Pugžlys, A. Baltuška, and S. Tzortzakis, Observation of extremely efficient terahertz generation from mid-infrared two-color laser filaments, Nat. Commun. **11**, 292 (2020).

[10] A. Englesbe, J. Elle, R. Reid, A. Lucero, H. Pohle, M. Domonkos, S. Kalmykov, K. Krushelnick, and A. Schmitt-Sody, Gas pressure dependence of microwave pulses generated by laser-produced filament plasmas, Opt. Lett. **43**, 4953 (2018).

[11] A. V. Mitrofanov, D. A. Sidorov-Biryukov, M. M. Nazarov, A. A. Voronin, M. V. Rozhko, A. B. Fedotov, and A. M. Zheltikov, Coherently enhanced microwave pulses from midinfrared-driven laser plasmas, Opt. Lett. **46**, 1081 (2021).

[12] A. Janicek, E. Thornton, T. Garrett, A. Englesbe, J. Elle, and A. Schmitt-Sody, Length dependence on broadband microwave emission from laser-generated plasmas, IEEE Trans. Plasma Sci. **48**, 1979 (2020).

[13] S. Tzortzakis, G. Méchain, G. Patalano, Y.-B. André, B. Prade, M. Franco, A. Mysyrowicz, J.-M. Munier, M. Gheudin, G. Beaudin, and P. Encrenaz, Coherent subterahertz radiation from femtosecond infrared filaments in air, Opt. Lett. **27**, 1944 (2002).

[14] C. D'Amico, A. Houard, M. Franco, B. Prade, A. Mysyrowicz, A. Couairon, and V. T. Tikhonchuk, Conical forward THz emission from femtosecond-laser-beam filamentation in air, Phys. Rev. Lett. **98**, 235002 (2007).

[15] P. Agostini and L. F. DiMauro, Atoms in high intensity mid-infrared pulses, Contemp. Phys. **49**, 179 (2008).

[16] N. E. Andreev, M. E. Veisman, S. P. Goreslavskii, and M. V. Chegotov, Residual electron

momentum and energy in a gas ionized by a short high-power laser pulse, Plasma Physics Rep. **27**, 278 (2001).

[17] P. Pulsifer, J. P. Apruzese, J. Davis, and P. Kepple, Residual energy and its effect on gain in a lyman-α laser, Phys. Rev. A **49**, 3958 (1994).

[18] B. M. Penetrante and J. N. Bardsley, Residual energy in plasmas produced by intense subpicosecond lasers, Phys. Rev. A **43**, 3100 (1991).

[19] See Supplemental Material at [*url will be inserted by publisher*] for additional context regarding the microwave generation mechanism, and ancillary results of the experiments and simulations.

[20] D. Marpaung, J. Yao, and J. Capmany, Integrated microwave photonics, Nat. Photon. **13**, 80 (2019).

[21] D. H. Auston and P. R. Smith, Generation and detection of millimeter waves by picosecond photoconductivity, Appl. Phys. Lett. **43**, 631 (1983).

[22] F. Sabath and E. Mokole, *Ultra-Wideband, Short-Pulse Electromagnetics 10* (Springer, 2014).

[23] H. Aggrawal, P. Chen, M. M. Assefzadeh, B. Jamali, and A. Babakhani, Gone in a picosecond: Techniques for the generation and detection of picosecond pulses and their applications, IEEE Microwave Magazine **17**, 24 (2016).

[24] J. S. Pearlman and G. H. Dahlbacka, Emission of rf radiation from laserproduced plasmas, J. Appl. Phys. **49**, 457 (1978).

[25] J. A. Aspiotis, N. Barbieri, R. Bernath, C. G. Brown, M. Richardson, and B. Y. Cooper, Detection and analysis of RF emission generated by laser-matter interactions, in *Enabling Technologies and Design of Nonlethal Weapons*, Vol. 6219, edited by G. T. Shwaery, J. G. Blitch, and C. Land, International Society for Optics and Photonics (SPIE, 2006) pp. 56 – 63.

[26] S. Varma, J. Spicer, B. Brawley, and J. A. Miragliotta, Plasma enhancement of femtosecond laser-induced electromagnetic pulses at metal and dielectric surfaces, Opt. Eng. **53**, 1 (2014).

[27] F. Consoli, V. T. Tikhonchuk, M. Bardon, P. Bradford, D. C. Carroll, J. Cikhardt, M. Cipriani, R. J. Clarke, T. E. Cowan, C. N. Danson, and et al., Laser produced electromagnetic pulses: generation, detection and mitigation, High Power Laser Sci. Eng. **8**, E22 (2020).

[28] J.-L. Dubois, F. Lubrano-Lavaderci, D. Raffestin, J. Ribolzi, J. Gazave, A. Compant La Fontaine, E. d'Humières, S. Hulin, P. Nicolaï, A. Poyé, and V. T. Tikhonchuk, Target charging in short-pulse-laser–plasma experiments, Phys. Rev. E **89**, 013102 (2014).

[29] A. Davidson, G. M. Petrov, B. Rock, P. Grugan, D. Gordon, B. Hafizi, A. Ting, and J. Peñano,

Dynamic sheath formation and sub-thz radiation from laser-metal interactions, Phys. Plasmas **27**, 073101 (2020).

[30] G. Andriukaitis, T. Balčiūnas, S. Ališauskas, A. Pugžlys, A. Baltuška, T. Popmintchev, M.-C. Chen, M. M. Murnane, and H. C. Kapteyn, 90 GW peak power few-cycle mid-infrared pulses from an optical parametric amplifier, Opt. Lett. **36**, 2755 (2011).

[31] C. A. Balanis, *Antenna Theory: Analysis and Design* (Wiley, 2016).

[32] E. Muehldorf, The phase center of horn antennas, IEEE Trans. Antennas Propag. **18**, 753 (1970).

[33] J. D. Jackson, *Classical Electrodynamics* (Wiley, 1998).

[34] P. Sprangle, J. R. Peñano, B. Hafizi, and C. A. Kapetanakos, Ultrashort laser pulses and electromagnetic pulse generation in air and on dielectric surfaces, Phys. Rev. E **69**, 066415 (2004).

[35] C. D'Amico, A. Houard, S. Akturk, Y. Liu, J. L. Bloas, M. Franco, B. Prade, A. Couairon, V. T. Tikhonchuk, and A. Mysyrowicz, Forward THz radiation emission by femtosecond filamentation in gases: theory and experiment, New J. Phys. **10**, 013015 (2008).

[36] S. Kalmykov, J. Elle, and A. Schmitt-Sody, Radiation emission at Langmuir frequency from laser wake in longitudinally stratified plasma column, Plasma Phys. Control. Fusion **62**, 115022 (2020).

[37] S. Kalmykov, J. Elle, and A. Schmitt-Sody, Reversal of laser wake phase velocity generates high-power broadband Cherenkov signal, Plasma Phys. Control. Fusion **63**, 045024 (2021).

[38] A. A. Voronin and A. M. Zheltikov, Laser-driven tunneling photocurrent as a source of mid-infrared to microwave multidecade supercontinua yoked to high-order harmonics, Phys. Rev. A **101**, 043813 (2020).

[39] A. Proulx, A. Talebpour, S. Petit, and S. Chin, Fast pulsed electric field created from the self-generated filament of a femtosecond Ti:sapphire laser pulse in air, Opt. Commun. **174**, 305 (2000).

[40] T. Garrett, J. Elle, M. White, R. Reid, A. Englesbe, R. Phillips, P. Mardahl, A. Schmitt-Sody, E. Thornton, J. Wymer, A. Janicek, and O. Sale, Generation of RF by atmospheric filaments, https://arxiv.org/abs/2102.12657 (2021), arXiv:2102.12657.

[41] D. Gordon, USNavalResearchLaboratory: SeaRay, Zenodo 10.5281/zenodo.4020488 (2020).

[42] M. Kolesik, J. V. Moloney, and M. Mlejnek, Unidirectional optical pulse propagation equation,

Phys. Rev. Lett. **89**, 283902 (2002).

[43] V. S. Popov, Tunnel and multiphoton ionization of atoms and ions in a strong laser field (Keldysh theory), Phys.-Uspekhi **47**, 855 (2004).

[44] A. Couairon and A. Mysyrowicz, Femtosecond filamentation in transparent media, Phys. Rep. **441**, 47 (2007).

[45] S. Zahedpour, S. W. Hancock, and H. M. Milchberg, Ultrashort infrared 2.5-11 micron pulses: spatiotemporal profiles and absolute nonlinear response of air constituents, Opt. Lett. **44**, 843 (2019).

[46] A. Sharma, M. N. Slipchenko, M. N. Shneider, X. Wang, K. A. Rahman, and A. Shashurin, Counting the electrons in a multiphoton ionization by elastic scattering of microwaves, Sci. Rep. **8**, 2874 (2018).

[47] A. Nguyen, K. J. Kaltenecker, J.-C. Delagnes, B. Zhou, E. Cormier, N. Fedorov, R. Bouillaud, D. Descamps, I. Thiele, S. Skupin, P. U. Jepsen, and L. Bergé, Wavelength scaling of terahertz pulse energies delivered by two-color air plasmas, Opt. Lett. **44**, 1488 (2019).

[48] V. Y. Fedorov and S. Tzortzakis, Extreme THz fields from two-color filamentation of midinfrared laser pulses, Phys. Rev. A **97**, 063842 (2018).

[49] M. Clerici, M. Peccianti, B. E. Schmidt, L. Caspani, M. Shalaby, M. Giguère, A. Lotti, A. Couairon, F. Légaré, T. Ozaki, D. Faccio, and R. Morandotti, Wavelength scaling of terahertz generation by gas ionization, Phys. Rev. Lett. **110**, 253901 (2013).

[50] V. Shumakova, S. Ališauskas, P. Malevich, C. Gollner, A. Baltuška, D. Khartashov, A. Zheltikov, A. Mitrofanov, A. Voronin, D. Sidorov-Biryukov, and A. Pugžlys, Filamentation of mid-IR pulses in ambient air in the vicinity of molecular resonances, Opt. Lett. **43**, 2185 (2018).

[51] L. V. Keldysh, Ionization in the field of a strong electromagnetic wave, JETP **20**, 1307 (1965).

[52] N. H. Burnett and P. B. Corkum, Cold-plasma production for recombination extreme-ultraviolet lasers by optical-field-induced ionization, J. Opt. Soc. Am. B **6**, 1195 (1989).

[53] W. Kruer, *The physics of laser plasma interactions* (CRC Press, 2003).

[54] C. Zhang, C.-K. Huang, K. A. Marsh, C. E. Clayton, W. B. Mori, and C. Joshi, Ultrafast optical field-ionized gases: A laboratory platform for studying kinetic plasma instabilities, Sci. Adv. **5**, eaax4545 (2019).

[55] H. Liang, D. L. Weerawarne, P. Krogen, R. I. Grynko, C.-J. Lai, B. Shim, F. X. Kärtner, and

K.-H. Hong, Mid-infrared laser filaments in air at a kilohertz repetition rate, Optica **3**, 678 (2016).

[56] A. V. Mitrofanov, A. A. Voronin, D. A. Sidorov-Biryukov, A. Pugžlys, E. A. Stepanov, G. Andriukaitis, T. Fl ory, S. Ališauskas, A. B. Fedotov, A. Baltuška, and A. M. Zheltikov, Mid-infrared laser filaments in the atmosphere, Sci. Rep. **5**, 8368 (2015).

[57] D. A. Romanov and R. J. Levis, Delayed ionization and excitation dynamics in a filament wake channel in a dense-gas medium, Phys. Rev. A **102**, 013110 (2020).

[58] W. Liu and S. L. Chin, Direct measurement of the critical power of femtosecond Ti:sapphire laser pulse in air, Opt. Express **13**, 5750 (2005).

Supplementary Material: Ultrabroadband microwave radiation from near and mid-infrared laser produced plasmas in air

Alexander Englesbe,[1] Jennifer Elle,[2] Robert Schwartz,[3] Travis Garrett,[2] Daniel Woodbury,[3] Dogeun Jang,[3] Ki-Yong Kim,[3] Howard Milchberg,[3] Remington Reid,[2] Adrian Lucero,[2] Daniel Gordon,[1] Ryan Phillips,[2] Serge Kalmykov,[2,4] and Andreas Schmitt-Sody[2]

[1]*Plasma Physics Division, Naval Research Laboratory, Washington, DC 20375*

[2]*High Power Electromagnetics Division, Air Force Research Laboratory, Kirtland AFB, NM 87117*

[3]*Institute for Research in Electronics and Applied Physics, University of Maryland, College Park, MD 20742*

[4]*Leidos Innovations Center, Albuquerque, NM 87106*

(Dated: July 8, 2021)

Abstract

In this supplementary document we have included some additional notes clarifying the microwave generation mechanism, the general protocol for performing the microwave receiver calibrations, and some comments on the laser propagation simulations. There are also additional experimental results that suggest a relationship between the input laser pulse energy and the peak microwave frequency due to the change in plasma length as the pulse energy increases. Finally, we present simulation results as a function of input pulse energy showing that the electron density due to the NIR laser pulses is consistently predicted to be much larger than that due to the MIR pulses.

I. LASER WAVELENGTH SCALING OF THE ELECTRON DRIFT VELOCITY

In high intensity laser-plasma interactions, the predominant wavelength λ_0 of the laser field is critical to the plasma generation and its subsequent evolution. For fixed intensity, the strong field ionization mechanism that produces the plasma changes character from non-adiabatic to adiabatic as the laser wavelength increases [1]. Once liberated from its bound state, a single free electron oscillating in a linearly polarized laser field has a cycle-averaged quiver energy

$$\epsilon_q = \frac{e^2 E_0^2}{4 m_e \omega_0^2} \propto I_0 \lambda_0^2 \tag{S1}$$

where E_0 is the laser electric field amplitude, I_0 is its intensity, and ω_0 is its angular frequency [2, 3]. In the non-relativistic semi-classical tunneling picture, an electron that tunnels into a free state at a time t_0 (where $t_0 = 0$ corresponds to the zero-crossing of the field oscillation) acquires a drift velocity $v_{drift} = 2\sqrt{\epsilon_q / m_e} \cos \omega_0 t_0$, with corresponding drift kinetic energy

$$\epsilon_{drift} = 2\epsilon_q \cos^2 \omega_0 t_0. \tag{S2}$$

If the field ionizes an electron at $\omega_0 t_0 = 0$, it would have a drift velocity of $2\epsilon_q$, while electrons born at the peak of the field ($\omega_0 t_0 = \pi/2$) have zero drift energy. The distribution of drift energies resulting from the variation of t_0 for all ionization events in the laser field is one significant factor that contributes to the total residual energy [4–7] of the electron population in the plasma. The sequence of processes by which the electrons re-distribute their residual energy in the plasma is not easily predicted [8] for an arbitrary laser pulse focused into a given gas. However the basic idea from Eqs. S1 and S2 – that $\epsilon_{drift} \propto \epsilon_q \propto I_0 \lambda_0^2$ – is sufficient to explain our experimental results and to describe the radiation mechanism.

Exploring the wavelength scaling of laser-plasma interactions experimentally is difficult. This is especially true for increasing λ_0 beyond 1 micron. In the case of sub-picosecond pulses, the availability of suitable laser gain media, and the historical inefficiency of optical parametric amplifiers (OPAs) has to date constrained the wavelength range of typical laser systems to the visible and near-infrared regime. Recent advances in fabricating nonlinear crystals and pump laser technology have made it possible to use OPAs to generate longer wavelength ultrashort pulses of sufficient power to ionize gases [9–11].

A. Estimate of the Plasma Current Rise Time

Using the values of peak intensity from the simulation results in Figure S3(c)-(d), we can estimate the value of the quiver energy using Eq. S1 to find $\epsilon_q \sim 9$ eV for $\lambda_0 = 0.8$ μm, while $\epsilon_q \sim 92$ eV for $\lambda_0 = 3.9$ μm. We can make a simple order of magnitude estimate of the rise time of the radial expansion that leads to the microwave radiation using these values of ϵ_q by calculating the acceleration, a, of electrons due to the radial pressure gradient, assuming a population of electrons carrying the quiver energy.

$$m_e n_e a = -\nabla p_e \simeq -k_B T_e \nabla n_e \simeq -\epsilon_q \nabla n_e, \tag{S3}$$

where m_e, n_e, p_e, and T_e are the electron mass, density, pressure, and temperature, respectively, while k_B is Boltzmann's constant. Eq. S3 assumes isothermal electrons $\nabla p_e = k_B T_e \nabla n_e$, which leads to

$$a = -\frac{\epsilon_q}{m_e}\left(\frac{\nabla n_e}{n_e}\right) \sim \frac{v_q^2}{2l}, \tag{S4}$$

where we have approximated $\nabla n_e / n_e \sim -1/l$ is the inverse gradient scale length in the radial direction, and $v_q = \sqrt{2\epsilon_q / m_e}$. From the simulation results in Figure 7(f) we estimate $l \sim 20$ μm. The time, t, required to perform an additional displacement l subject to constant acceleration a is

$$\begin{aligned} t = \frac{2l}{v_q} &= 22 \text{ ps for } \epsilon_q = 9 \text{ eV} \\ &= 7 \text{ ps for } \epsilon_q = 92 \text{ eV} \end{aligned}$$

which agrees to an order of magnitude with microwave field periods corresponding to frequencies in the 10's of GHz which we have measured. The weak dependence of t on ϵ_q may

be reflected in Figure S1(c), as $\lambda_{\mu W}^{max}$ is typically smaller (thus the frequency is higher) for the MIR laser pulses relative to the NIR pulses.

This simplistic calculation is only meant to be illustrative, and neglects electron collisions and the electrostatic field that arises due to the excursion of electrons from the plasma surface, leaving it positively charged. The collision rate and plasma frequency (the response rate of the plasma to the charge separation) both occur on single picosecond timescales (see for example [12]) meaning that the expansion wave should be strongly damped. Further, most of the electrons are born cold near the peak of the laser field oscillations, and the proportion of the population that has energy on the order of ϵ_q is very small, in spite of the hydrodynamic notions invoked in Eqs. S3 and S4. An accurate calculation of how the small number of electrons with energy on the order of ϵ_q translates to longitudinal surface current and microwave radiation will require a fully kinetic description of the system, which in practice means particle-in-cell (PIC) simulations of sufficient spatial and temporal size. Recent theoretical analysis of plasma generated by filamentation of NIR laser pulses in high pressure gas found that thermal expansion of the electron population leads to the creation of a radial electric field [13], such as we have proposed here. The model accounts for only the radial dimension, and calculations are made for argon at 60 atmospheres instead of air at one atmosphere. However, it shows that the plasma dynamics and collisional kinetics after the passage of the laser pulse are non-trivial in the sense that there are multiple phases to the time evolution of the plasma.

II. ADDITIONAL DETAILS FOR METHODS

A. Absolute Calibration of the Electric Field Spectra

The absolute value of the free space electric field amplitude at the antenna aperture may be calculated based on the definition of the antenna factor. It is the ratio of the aperture electric field amplitude to the voltage produced at its terminals.

$$E(f) = \frac{V_m(f)}{X(f)} \sqrt{\frac{4\pi\eta_0 f^2}{c^2 Z_R G(f)}}, \tag{S5}$$

where $X(f)$ is the cable and oscilloscope calibration factor, and $G(f)$ is the antenna gain. $V_m(f)$ is the real part of the Fourier transform (voltage spectrum) of the waveform trace

measured on the oscilloscope, and η_0, f, c, and Z_R are the impedance of free space, frequency, speed of light in vacuum, and real part of the load impedance, respectively. $X(f)$ is found by calculating the ratio of the voltage spectrum measured from the reference noise source to the known voltage spectrum that it produces,

$$X(f) = \frac{V_{m,ref}(f)}{V_{ref}(f)}. \tag{S6}$$

The quantity V_m/X is the voltage the incident microwave field induces on the antenna terminals. Any radiation losses (for example ohmic losses) incurred in the antenna structure are accounted for in the gain measurement of $G(f)$. Equation S5 assumes that the antenna is in the far field region of the microwave source, and that negligible radiation enters the antenna through its side lobes.

B. SeaRay Simulations

Assumption of cylindrical symmetry in the laser propagation simulations is permissible even though the peak power of the NIR pulses is many times the self-focusing critical power, P_{cr} where the ratio of input laser power $P/P_{cr} = 1$ determines the threshold for filamentation. The relatively tight geometric focusing prevents multi-filamentation, which would violate the assumption of cylindrical symmetry. Images of the plasma fluorescence given in Supplementary Section III show that multi-filamentation does not occur for the NIR laser pulses.

Some additional factors involving the dynamics of the air plasma that the propagation simulations do not capture include the creation of a secondary electron population due to impact ionization for the MIR laser field, decay of the plasma by recombination, and the precise location within the plasma of the microwave critical surface from which the radiation fields can propagate. These phenomena may influence the microwave generation by creating additional charge carriers, placing a maximum limit on the plasma lifetime, and determining the coupling efficiency of the longitudinal surface current to radiating electromagnetic fields, respectively.

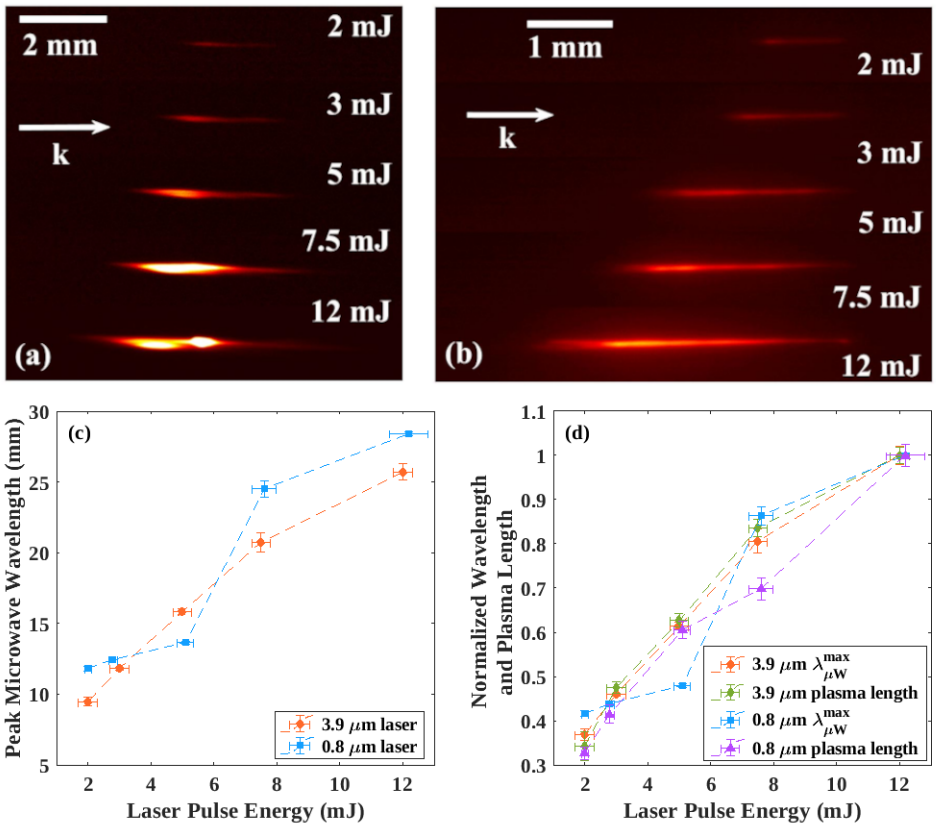

FIG. S1. Colorized images of the plasma fluorescence as a function of laser pulse energy for the (a) MIR laser, and (b) NIR laser. The arrows indicate the direction of laser propagation. (c) Free space microwave wavelength corresponding to the peak of the frequency spectra in Figure 5 as a function of energy for the MIR laser pulses (orange circles) and NIR laser pulses (blue squares). (d) The functional dependence of the length of the plasma fluorescence (3.9 μm – green diamonds, 0.8 μm – purple triangles) and the peak microwave wavelength ($\lambda_{\mu W}^{max}$) on laser pulse energy for both MIR and NIR experiments. The error bars on $\lambda_{\mu W}^{max}$ are the standard deviation of $\lambda_{\mu W}^{max}$ for three different fitting functions applied to each microwave spectrum. The error bars on the relative plasma length are the standard deviation measured from ten images of each case. The laser energy error bars estimate the shot-to-shot pulse energy fluctuation.

III. ADDITIONAL EXPERIMENTAL SUPPORT FOR THE PROPOSED RADIATION GENERATION MECHANISM

A. Comparison of Relative Plasma Length and Peak Microwave Wavelength

The basis for our claim that the plasma length influences the microwave frequency content is given in Figure S1. It compares the peak microwave wavelengths extracted from the spectra of Figure 5 of the main text to side view images of the visible plasma fluorescence, which we use to approximate the plasma length.

Figures S1(a) and S1(b) show the images of the plasma fluorescence for the MIR laser and NIR laser, respectively. Qualitatively, the MIR laser pulses in this experiment produce air plasmas that are larger and have brighter fluorescence. However, a quantitative comparison between Figures S1(a) and S1(b) is not possible because the images were taken with different cameras. The difference in brightness suggests that the energy deposited in the MIR laser plasma is relatively greater, which may mean that its electrons are hotter, although confirmation of this would require a quantitative diagnostic, such as optical emission spectroscopy.

Figure S1(c) quantifies the laser energy dependence of the predominant frequency components of the microwave radiation. We have estimated the peak frequency from each spectrum in Figure 5 for both laser wavelengths, and calculated the corresponding peak microwave wavelength ($\lambda_{\mu W}^{max} = c/f_{\mu W}^{max}$). The values of $\lambda_{\mu W}^{max}$ for the MIR and NIR cases are similar even though the appearance of the plasmas produced by each laser are different. Quantitative comparison of $\lambda_{\mu W}^{max}$ and the length of the plasma fluorescence could be misleading because the space occupied by the electrons is not necessarily equivalent to the volume containing the fluorescing heavy species.

Instead, Figure S1(d) compares the functional dependence of $\lambda_{\mu W}^{max}$ and the length of the plasma fluorescence on laser energy. By normalizing the length and $\lambda_{\mu W}^{max}$ values for both laser wavelengths in Figure S1(d), we see linear increases with nearly the same slope. Presenting the data in this manner relies on the linearity of each camera's response, as opposed to their absolute sensitivities. The strong correlation between $\lambda_{\mu W}^{max}$ and the relative plasma length leads us to conclude that the current modulation caused by the plasma's longitudinal profile is an operative timescale of the radiation generation.

B. Discriminating the Angular Stratification of the Microwave Spectrum from its Variation with the Plasma Length

The microwave spectra in Figure 5 and therefore peak wavelengths analyzed in Figure S1 were recorded at an angular position of $\theta = 90°$. However, Figure 3 of the main text clearly shows that there is an angular dependence to the spectrum, since we measure increasingly forward-directed radiation with higher frequency antennas. Since we claim that the spectrum also simultaneously depends on the plasma length, it is important to establish that our interpretation of Figures 5 and S1 does not conflate changes in the spectrum due to the angular dependence with changes in the inherent frequency content due to the length as it increases with laser energy. Indeed, an existing narrowband measurement at 91 GHz with extended filament plasmas shows that the plasma length changes the shape of the radiation pattern [14].

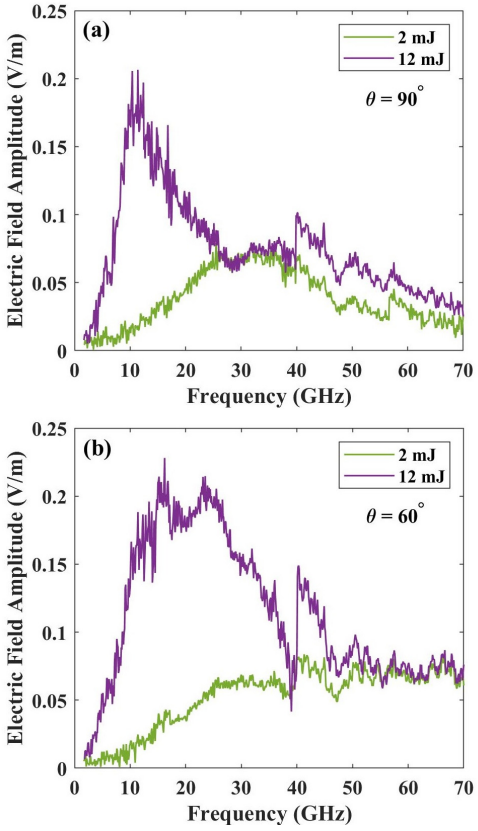

FIG. S2. Comparison of the MIR-generated microwave spectrum for laser pulse energies of 2 mJ and 12 mJ at antenna angular positions of (a) $\theta = 90°$, and (b) $\theta = 60°$.

It is simple to resolve this issue by demonstrating that the laser energy-dependent peak frequency shift seen in Figure 5 may be found at multiple emission angles. Figure S2 shows the microwave spectra for MIR laser energies of 2 mJ and 12 mJ found at $\theta = 90°$ and $\theta = 60°$. Figure S2(b) shows that there is more high frequency content closer to the laser axis at both 2 mJ and 12 mJ. The emission of higher frequencies closer to the laser axis has been documented before [15, 16]. However at both $\theta = 60°$ and $\theta = 90°$, the radiation from the plasma produced with 12 mJ pulses consists of more low-frequency content than that at 2 mJ. This supports the notion that the range of frequencies the plasma is able to radiate depends on the longitudinal extent of the plasma. The plasma length may also determine the angles at which the different frequency components propagate outward from the source, but Figure S2 demonstrates that we can discriminate between these two aspects of the radiation in our explanation of the generation mechanism.

C. Note on Microwave Radiation from Longitudinally Short Sparks versus Extended Filament Plasmas

It is important to reconcile the strong dependence of the microwave frequency content on plasma length we observe in the 2-70 GHz range in these experiments with the weak plasma length dependence over 2-14 GHz in our prior experiments [16]. The present experiments deal with millimeter-scale plasmas, as shown in Figure S1, whereas the prior measurements at 2-14 GHz were performed with centimeter to meter-scale laser plasmas.

In Figure S1 we see that changing the plasma length by a factor of about 3 shifts the peak microwave wavelength also by a factor of 3, while the prior measurements see a $\sim 10\%$ wavelength shift when the plasma elongates by a factor of 6. A preliminary explanation of the discrepancy is that not all of the microwave frequency components constructively interfere with uniform frequency-dependent gain when the plasma is long. This is to say that the microwaves may exhibit phase matching requirements.

When the plasma is short, the impulsive current driven by the electron expansion wave terminates quickly as the laser pulse diffracts after the focal volume. In this case the microwave field must transition to free radiation before preferential constructive interference of the low-frequency components dominates, producing pulses with the nearly two decades of bandwidth we see in these experiments. The prior long plasma measurements suggest, with

support from modeling, that the microwave field strength from 2-14 GHz grows with plasma length due to the fact that the electron expansion wave is coherent with the laser envelope (that is, both propagate at the laser group velocity) and therefore that the microwave field constructively interferes with itself as the laser pulse and the current source move together through the plasma. Our ongoing work seeks to explain in detail why the low frequencies interfere more efficiently when the plasma is longer.

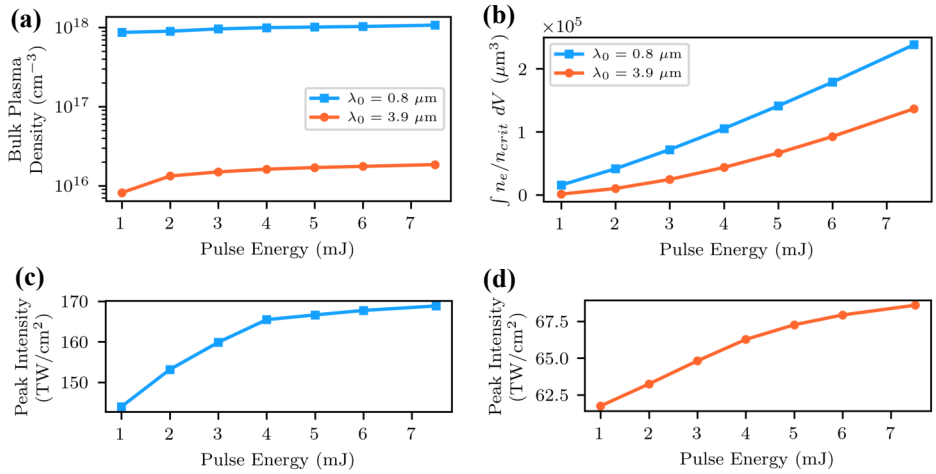

FIG. S3. (a) Simulated bulk electron density as a function of laser pulse energy for the NIR and MIR laser pulses. (b) Total free charge calculated by integrating the plasma density in space, normalized to the critical electron density for each laser wavelength. The peak intensities of the laser pulses as a function of input energy are given in (c) for $\lambda_0 = 0.8\ \mu$m, and (d) for $\lambda_0 = 3.9\ \mu$m.

IV. SIMULATED LASER PULSE ENERGY DEPENDENCE OF ELECTRON DENSITY AND PEAK INTENSITY

Trends of the simulated electron density and peak laser intensity as a function of input pulse energy are given in Figure S3. The average electron density in the core of the plasma, shown in Figure S3(a), is consistently almost two orders of magnitude greater for the NIR pulses than the MIR pulses. The plasma for both laser wavelengths is obviously overdense to microwaves. This further supports the notion that the generation mechanism relies on a surface current.

The cause for the difference in electron density for the two laser wavelengths may be explained using Figure S3(b). Integrating the electron density over all space gives the total free charge. This value is normalized in each case to the appropriate value of the critical electron density, $n_{cr} = 4\pi^2 c^2 \epsilon_0 m_e (e\lambda_0)^{-2}$, for each laser wavelength. For $\lambda_0 = 0.8$ μm, $n_{cr} = 1.7 \times 10^{21}$ cm^{-3}, while for $\lambda_0 = 3.9$ μm, $n_{cr} = 7.3 \times 10^{19}$ cm^{-3}. The quantity $\int n_e/n_{cr}\ dV$ is related to the total phase that the pulses accumulate after propagating through the plasma. Figure S3(b) indicates that ionization occurs such that the MIR and NIR laser pulses both acquire similar phase from the plasma. For the NIR pulses only, the value of n_e/n_{cr} must be greater to counteract self-focusing, which explains the larger value of $\int n_e/n_{cr}\ dV$ for $\lambda_0 = 0.8$ μm.

We also see intensity clamping of the NIR pulses in Figure S3(c), which is a consequence of propagation above P_{cr} that we expect to accompany the transverse pulse collapse. For $\lambda_0 = 0.8$ μm in atmosphere, the maximum intensity achievable is on the order of 10^{14} W/cm^2 [17] when the pulse exceeds P_{cr}. We see in Figure S3(c) that the NIR pulses experience clamping at this value of intensity. Whereas the MIR pulses do not experience clamping and exhibit a more linear increase in peak intensity with increasing pulse energy. The case of the NIR 5 mJ pulse in Figure 7(a),(b) of the main text is a demonstration of the collapse. It occurs for all pulses above P_{cr}, which is to say all values of pulse energy with $\lambda_0 = 0.8$ μm used in the experiments and simulations, and none for $\lambda_0 = 3.9$ μm. Assuming good beam quality, P_{cr} in atmosphere at $\lambda_0 = 0.8$ μm is about 5-10 GW, and the lowest power NIR pulse at 1 mJ, 50 fs has peak power of 20 GW. Scaling P_{cr} by λ_0^2, the critical power at $\lambda_0 = 3.9$ μm is about 150-250 GW, and the highest power MIR pulse in the experiments at 12 mJ, 100 fs has 120 GW peak power.

---

[1] L. V. Keldysh, Ionization in the field of a strong electromagnetic wave, JETP **20**, 1307 (1965).

[2] P. Agostini and L. F. DiMauro, Atoms in high intensity mid-infrared pulses, Contemp. Phys. **49**, 179 (2008).

[3] W. Kruer, *The physics of laser plasma interactions* (CRC Press, 2003).

[4] N. H. Burnett and P. B. Corkum, Cold-plasma production for recombination extreme-ultraviolet lasers by optical-field-induced ionization, J. Opt. Soc. Am. B **6**, 1195 (1989).

[5] B. M. Penetrante and J. N. Bardsley, Residual energy in plasmas produced by intense subpicosecond lasers, Phys. Rev. A **43**, 3100 (1991).

[6] P. Pulsifer, J. P. Apruzese, J. Davis, and P. Kepple, Residual energy and its effect on gain in a lyman-α laser, Phys. Rev. A **49**, 3958 (1994).

[7] N. E. Andreev, M. E. Veisman, S. P. Goreslavskii, and M. V. Chegotov, Residual electron momentum and energy in a gas ionized by a short high-power laser pulse, Plasma Physics Rep. **27**, 278 (2001).

[8] C. Zhang, C.-K. Huang, K. A. Marsh, C. E. Clayton, W. B. Mori, and C. Joshi, Ultrafast optical field-ionized gases: A laboratory platform for studying kinetic plasma instabilities, Sci. Adv. **5**, eaax4545 (2019).

[9] G. Andriukaitis, T. Balčiūnas, S. Ališauskas, A. Pugžlys, A. Baltuška, T. Popmintchev, M.-C. Chen, M. M. Murnane, and H. C. Kapteyn, 90 GW peak power few-cycle mid-infrared pulses from an optical parametric amplifier, Opt. Lett. **36**, 2755 (2011).

[10] H. Liang, D. L. Weerawarne, P. Krogen, R. I. Grynko, C.-J. Lai, B. Shim, F. X. Kärtner, and K.-H. Hong, Mid-infrared laser filaments in air at a kilohertz repetition rate, Optica **3**, 678 (2016).

[11] A. V. Mitrofanov, A. A. Voronin, D. A. Sidorov-Biryukov, A. Pugžlys, E. A. Stepanov, G. Andriukaitis, T. Fl ory, S. Ališauskas, A. B. Fedotov, A. Baltuška, and A. M. Zheltikov, Mid-infrared laser filaments in the atmosphere, Sci. Rep. **5**, 8368 (2015).

[12] P. Sprangle, J. R. Peñano, B. Hafizi, and C. A. Kapetanakos, Ultrashort laser pulses and electromagnetic pulse generation in air and on dielectric surfaces, Phys. Rev. E **69**, 066415 (2004).

[13] D. A. Romanov and R. J. Levis, Delayed ionization and excitation dynamics in a filament wake channel in a dense-gas medium, Phys. Rev. A **102**, 013110 (2020).

[14] C. D'Amico, A. Houard, M. Franco, B. Prade, A. Mysyrowicz, A. Couairon, and V. T. Tikhonchuk, Conical forward THz emission from femtosecond-laser-beam filamentation in air, Phys. Rev. Lett. **98**, 235002 (2007).

[15] A. Englesbe, J. Elle, R. Reid, A. Lucero, H. Pohle, M. Domonkos, S. Kalmykov, K. Krushelnick, and A. Schmitt-Sody, Gas pressure dependence of microwave pulses generated by laser-produced filament plasmas, Opt. Lett. **43**, 4953 (2018).

[16] A. Janicek, E. Thornton, T. Garrett, A. Englesbe, J. Elle, and A. Schmitt-Sody, Length

dependence on broadband microwave emission from laser-generated plasmas, IEEE Trans. Plasma Sci. **48**, 1979 (2020).

[17] W. Liu and S. L. Chin, Direct measurement of the critical power of femtosecond Ti:sapphire laser pulse in air, Opt. Express **13**, 5750 (2005).

DISTRIBUTION LIST

DTIC/OCP
8725 John J. Kingman Rd, Suite 0944
Ft Belvoir, VA 22060-6218 1 cy

AFRL/RVIL
Kirtland AFB, NM 87117-5776 1 cy

Official Record Copy
AFRL/RDHP/Andreas Schmitt-Sody 1 cy